AI-Powered Biomolecular-Specific and Label-Free Multispectral Imaging Rapidly Detects Malignant Neoplasm in Surgically Excised Breast Tissue Specimens

Rishikesh Pandey, PhD; David Fournier, MS; Gary Root, MS, MBA; Machele Riccio, BS; Aditya Shirvalkar, MS; Gianfranco Zamora, BA; Noel Daigneault; Michael Sapack, BS; Minghao Zhong, MD, PhD; Malini Harigopal, MD

***Context.*—Repeated surgery is necessary for 20% to 40% of breast conservation surgeries owing to the unavailability of any adjunctive, accurate, and objective tool in the surgeon's hand for real-time margin assessment to achieve the desired balance of oncologic and cosmetic outcomes.**

***Objective.*—To assess the feasibility of using a multispectral autofluorescence imaging device for discriminating malignant neoplasm from normal breast tissue in pathology as a critical step in the development of a device for intraoperative use, and to demonstrate the device's utility for use in processing and prioritizing specimens during frozen section and in the pathology grossing room.**

***Design.*—We performed a preliminary assessment of our device, called the TumorMAP system, on 172 fresh tissue blocks from 115 patients obtained from lumpectomy specimens at the time of initial gross examination and compared the device results with gold standard pathology evaluation.**

***Results.*—The preliminary results demonstrate the potential of our device in detecting breast cancer in fresh tissue samples with a sensitivity of 82%, a specificity of 91%, a positive predictive value of 84%, and a negative predictive value of 89%.**

***Conclusions.*—Our results suggest that the TumorMAP system is suitable for the detection of malignant neoplasm in freshly excised breast specimens and has the potential to evaluate resection margins in real time.**

(*Arch Pathol Lab Med.* doi: 10.5858/arpa.2022-0228-OA)

There are approximately 300 000 women per year in the United States alone who are diagnosed with breast cancer[1] and a significant number of patients undergo breast-conserving surgery (BCS) as part of the standard of care for the treatment for the disease. BCS followed by postoperative radiation provides the same long-term survival as mastectomy[2] and is recommended over mastectomy.[3] Studies have shown that repeated surgery is necessary in 20% to 40% of BCS cases after the postoperative histopathologic examination of positive margins.[4–6] The standard of care for identifying cancerous tissue at the margins during BCS remains the gross visual examination of the ex vivo lumpectomy specimen, palpation of the ex vivo lumpectomy specimen, and palpation of the lumpectomy cavity. The effectiveness of visual/palpation techniques is limited by the human senses and individual surgical expertise and varies depending on the cancer type. Frozen section analysis, which is practiced clinically for other cancers in an intraoperative setting, is considered less suitable for BCS specimens owing to adipose-induced artifacts, high costs, low tissue sampling percentage, and the requirement of dedicated laboratory staff near the operating room (OR). While various technologies have been proposed for intraoperative assessment,[7] including for breast neoplasm,[8] no technique has been widely adopted by surgeons so far for use in the OR for margin assessment during surgery. Consequently, there is a large unmet need for an accurate and real-time intraoperative tool for cancer margin detection.

Advanced optical imaging approaches have been proposed for the determination of margin status.[9] These include the use of fluorescence,[10–14] diffuse reflectance imaging,[15] Raman spectroscopy,[16,17] hyperspectral imaging,[18] optical coherence tomography,[19] and quantitative microelastography.[20] Among the optical techniques, fluorescence offers a straightforward approach to providing diagnostic information that is interpretable and attributable to known biology. More recently, fluorescence-guided surgery (FGS) has been used for the detection of cancer during surgery and margin assessment.[21,22] Cancer imaging using FGS typically involves the use of nonspecific or targeted fluorescent imaging agents/tracers such as those that bind to cell surface carbohydrates, free proteins, specific enzymes, or expressed cell surface receptors of cancer cells. However, the clinical adaptation of FGS has been hindered owing to limited

Accepted for publication September 20, 2022.

From the Department of Research, CytoVeris Inc, Farmington, Connecticut (Pandey, Fournier, Root, Riccio, Shirvalkar, Zamora, Daigneault, Sapack); and the Department of Pathology, Yale School of Medicine, New Haven, Connecticut (Zhong, Harigopal).

Pandey, Fournier, Root, Shirvalkar, Zamora, and Sapack are current employees of CytoVeris Inc. Riccio has stock option in CytoVeris Inc as a former employee. The other authors have no relevant financial interest in the products or companies described in this article.

Corresponding author: Malini Harigopal, MD, Department of Pathology, Yale School of Medicine, 430 Congress Ave, New Haven, CT 06520 (email: malini.harigopal@yale.edu).

photostability, concern over chemical toxicity, poor tumor to background ratio, and the need for administration of a tracer before surgery.

Label-free approaches offer significant advantages to patients by avoiding potential toxicologic issues, US Food and Drug Administration (FDA) approval of contrast agents, the cost of contrast agents, and increased surgical time associated with administering fluorescence imaging agents. In contrast to the use of tracers, the endogenous autofluorescence (AF) signatures of tissue offer useful information that can be mapped to the molecular, metabolic, and morphologic attributes of a biological specimen[23] and have therefore been used for diagnostic purposes. Biomolecules such as tryptophan, collagen, elastin, nicotinamide adenine dinucleotide, flavin adenine dinucleotide, and porphyrins present in tissue provide discernible and repeatable AF spectral patterns[24] that can be interpreted as a "biomolecular optical fingerprint." Biomolecular changes occurring in the cell and tissue microenvironment during pathologic processes and disease progression result in alterations in the amount and distribution of endogenous fluorophores and form the basis for diagnosis. In the oncologic surgical setting, many approaches that leverage AF attributes of the tissue have been proposed for neoplasm detection including breast cancer,[25] brain cancer,[26] bladder cancer,[27] oral cancer,[28] and lung cancer.[29] In addition to fluorescence intensities, fluorescence lifetime imaging (FLIM), which measures the lifetime of the intrinsic fluorophores, has been demonstrated to discern positive breast cancer margin in a preclinical study[12] and visual inspection of oral cancers during transoral robotic surgery.[30] However, FLIM devices require 1 or more pulsed laser sources, a very complex detection and read-out system, and therefore may not be compatible with the surgical workflow and may also be cost-prohibitive.

While tissue AF spectroscopy has been proposed and demonstrated previously for cancer detection, its practical use has been hindered primarily owing to limited diagnostic accuracy and slow processing time, and therefore has not been suitable for real-time surgical use. The scanning speed has been primarily limited by the traditional use of fiber probes with single-point measurement capability. The use of AF imaging, which marries biomolecular information with spatial mapping information, allows increased information content to be captured and processed. Further, most of the prior studies have used either visible or UVA (ultraviolet A, 315–400 nm) for fluorescence excitation and the use of UVC has been limited by the limited availability, cost, and complexity of suitable excitation sources. The advent of UVC light-emitting diodes (LEDs) and advancements in UV optical technology have recently allowed full exploitation of the rich fluorescence from endogenous biomolecular fluorophores embedded in tissues. This enables optimal excitation of certain biomolecules and efficient and selective collection of the emitted light.

Artificial intelligence (AI) and machine learning (ML) have enabled analyzing and retrieving the nearly imperceivable and subtle differences in complex data sets that are beyond human interpretability.[31,32] AI has also been proposed for clinical uses including cancer diagnosis,[33] radiology,[34] pathology,[35] and even risk prediction.[36] With the recent FDA approval of AI-based Paige Prostate to detect prostate cancer from digitally scanned slides, AI and ML hold promise to assist pathologists in their practice.[37] We leverage the recent advancements in AI to capture latent biomolecular and morphologic differences that are encoded in multispectral images. We hypothesize that UV-excited multispectral AF images of tissue comprise more information than is readily apparent, and this information can be leveraged by using advanced AI/ML approaches, paving the way for clinical application.

In this proof-of-concept study, we sought to determine if multispectral AF imaging when combined with advanced AI/ML approaches can detect malignant neoplasm in real-time from excised breast tissue blocks. We performed a preliminary assessment of our TumorMAP system (CytoVeris Inc) powered with OncoSight AI classifier (CytoVeris Inc), on 172 tissue blocks originated from 115 patients and compared the results with the hematoxylin-eosin (H&E) evaluations of the same tissue block. The preliminary results are promising in detecting cancer with a sensitivity of 82%, specificity of 91%, a positive predictive value of 84%, and a negative predictive value of 89%. Owing to the widefield and single-shot imaging with no sample preparation requirement, this preclinical study in the grossing laboratory forms the basis for a feasibility study in the OR. We intend to validate the use of an intraoperative imaging system for the ex vivo examination of excised specimens in a future feasibility study. If validated, our device will accurately detect whether cancer is present on the specimen surface, enabling the surgeon to resect additional tissue if the resection is incomplete, thereby obviating the need for re-excision of positive margins found subsequently on pathologic examination. We intend to test this technology for other types of cancer surgery, which are typically performed with minimally invasive/robotic techniques. Our long-term goal is to develop an optical imaging probe-based platform to provide the surgeon with additional intraoperative visualization of cancer in vivo.

MATERIALS AND METHODS

TumorMAP

The TumorMAP system relies on the intrinsic tissue AF of various endogenous fluorophores found in different tissue types. The TumorMAP system leverages changes in a matrix of these fluorophores that form the basis for tissue analysis and discerning cancerous tissue. It uses multispectral excitation and detection not only to increase the information content but also to produce differential and specific emission signals. This widefield system captures multispectral images and does not require any X-Y movement or scanning to evaluate the specimen. The multi-excitation in the UV region and multidetection strategy allows the acquisition of comprehensive and rich biomolecular and morphologic information from both cells and the extracellular matrix. The TumorMAP system is contact-free, fully automated, does not require sample preparation, and provides tissue imaging in quasi–real-time.

Tissue Collection

This preclinical research study was approved by the Institutional Review Board of Yale Smilow Cancer Center (New Haven, Connecticut). Under the study protocol, following tissue excision during breast lumpectomy surgery, the fresh breast tissue specimens are sent to the surgical pathology laboratory where they are inked and grossed by the pathology assistant or resident per the institution's established surgical pathology process. After grossing into blocks and before tissue fixation, a selected set of the tissue blocks were imaged with the TumorMAP system. To maintain tissue integrity and to preserve the routine clinical workflow, no chemicals or other processing steps were applied to the tissue block. The total imaging time for a tissue block was only

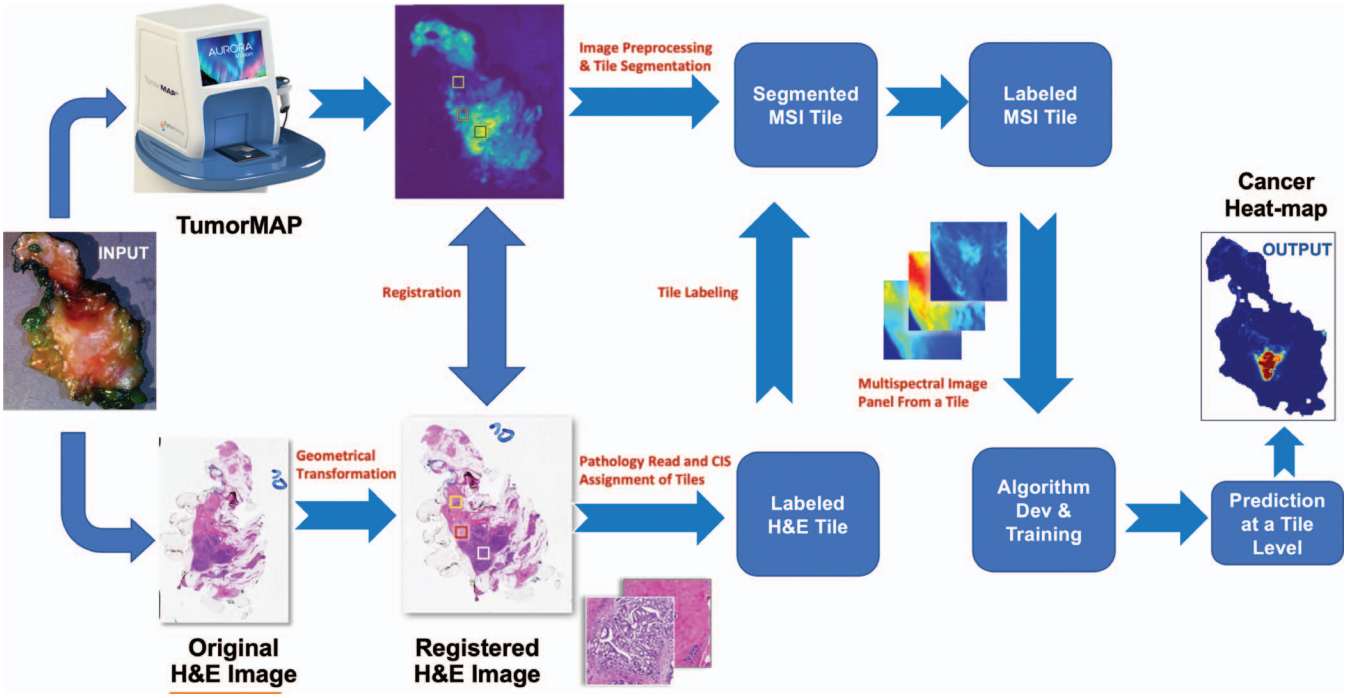

Figure 1. *Tissue scanning and algorithm training workflow. Abbreviations: CIS, cancer infiltration score; Dev, development; H&E, hematoxylin-eosin; MSI, multispectral image.*

~32 seconds, ensuring that no undue drying of specimens took place during imaging, and that the process did not impact the cycle time of the tissue grossing to fixation process. After the imaging, the tissue blocks were sent through the routine formalin-fixation and paraffin-embedding (FFPE) process. The corresponding H&E slides of the tissue blocks imaged by the TumorMAP system were digitized and used for histopathologic investigation and label creation for algorithm development. All patient identifying data were de-identified for this study.

Algorithm Training

A subset of multispectral images was combined in a certain way to generate a composite image for registration with H&E images. The original H&E image of the tissue block was geometrically transformed to match with AF composite image measured from the same block; 2 mm × 2 mm "tiles" containing areas of high tissue homogeneity on the H&E images were identified and transcribed onto the UV composite image. Each tile comprises 50 × 50 = 2500 image pixels, each of which represents a measure of the "biomolecular optical fingerprint" of the tissue at that spatial location. The selected homogeneous areas from the H&E images were then cropped and independently scored by 2 board-certified pathologists.

The primary inclusion criterion for malignant cases was that the 2 mm × 2 mm "tiles" should have a "cancer infiltration score" (CIS) of 80% or greater and no case selections were made on the basis of cancer type, grades or stages, receptor status, neoadjuvant status, or any other patient metadata. The benign category was represented by tiles that included different types of benign tissue with homogeneity of 80% or greater as ground truth.

The 2 pathologists examined the targeted homogeneous areas (tiles) to identify the tissue types and scored the tiles for tissue identification. In the case of a cancer tile, a CIS was also noted. The CIS is defined as the percentage area of the tile that has cancer or is affected by the cancer field, including local cancer-associated desmoplasia. In case of a discrepancy between the 2 pathologists about the tissue-type assignment, a joint scoring was performed to reach a consensus. Also, if the 2 pathologists' scores were discordant by 15% or more, it was rescored by the same 2 pathologists to reach a consensus. A mean infiltration score was used for training the algorithm. The detailed tissue processing and algorithm training workflow is illustrated in Figure 1. The system was trained and tested by using a leave-one-patient-out validation process, and a CIS of 80% or greater was used for the training.

RESULTS

We measured multispectral AF images of breast tissue specimens, which resulted in 417 tiles obtained from 115 patients in the age range of 34 to 93 years. These specimens comprise both benign and cancerous tissues. The benign category includes adipose, fibrous, glandular, along with different types of other nonmalignant tissues such as desmoplasia and inflammation (not associated with fat necrosis). Of these 417 tiles, the pathologists identified 156 tiles containing cancer from 55 patients. The Table shows the patient demographic details, cancer types, Nottingham score, cancer stage, estrogen receptors, human epidermal growth factor receptor 2 (HER2) scores, and neoadjuvant therapy status. Of the 55 patients' cancer tiles, the pathologic read indicated N = 44 patients with primarily invasive ductal carcinoma (IDC), N = 7 with only ductal carcinoma in situ (DCIS), and N = 4 with invasive lobular carcinoma (ILC). Notably, this cancer type distinction is based on postoperative histopathology, not on the diagnosis before surgery. As evident in the Table, the patients have significant diversity in Nottingham scores, cancer stages, estrogen receptor and HER2 expression levels, and neoadjuvant therapy status.

We developed an ensemble classifier consisting of multiple base learners that were then combined through a meta learner for final classification. The classifier was tested by using leave-one-patient-out cross-validation. Figure 2 illustrates the confusion matrix reflecting the performance of the OncoSight AI classifier. Of a total of 417 labeled tiles, 156 tiles contained cancer, and the remaining 261 tiles were

Patient Demographic Data and Details of the Measured Tissues		
	No. of Patients	Percentage[a]
Patient information for all tissue blocks		
Nonmalignant	60	52
Cancer	55	48
Patient information for cancer-only blocks		
Age, y		
Mean	64	
Postmenopausal status		
Yes	41	75
No	13	23
Not known	1	2
Race		
White	49	89
Black or African American	5	9
Asian	1	2
Cancer type		
IDC	44	80
DCIS	7	13
ILC	4	7
Nottingham score		
Grade I (3–5)	11	20
Grade II (6–7)	29	53
Grade III (8–9)	10	18
NA (DCIS)	5	9
Stage		
T1	35	64
T2	14	25
T3	1	2
Tis	5	9
ER (Allred)		
Negative (0–2)	1	2
Positive (3–8)	54	98
HER2		
Negative (0)	20	36
Negative (1)	14	26
Equivocal (2)	15	27
Positive (3)	0	0
NA	6	11
Neoadjuvant therapy status		
Yes	3	5
No	52	95

Abbreviations: DCIS, ductal carcinoma in situ; ER, estrogen receptor; HER2, human epidermal growth factor receptor 2; IDC, invasive ductal carcinoma; ILC, invasive lobular carcinoma; NA, not applicable.

[a] Calculated from a total patient number of 115 and 55 for all tissue blocks and cancer-only tissue blocks, respectively.

labeled as benign as per histologic ground truth. Our classifier yielded a sensitivity of 82%, specificity of 91%, positive predictive value of 84%, and negative predictive value of 89% with cancer prevalence of 38%. We also calculated the Matthews correlation coefficient (MCC), which is known as one of the reliable and robust performance metrics of a binary classifier and has recently been recommended over diagnostic odds ratio.[38] A coefficient of +1 represents a perfect prediction and our MCC value was 0.73.

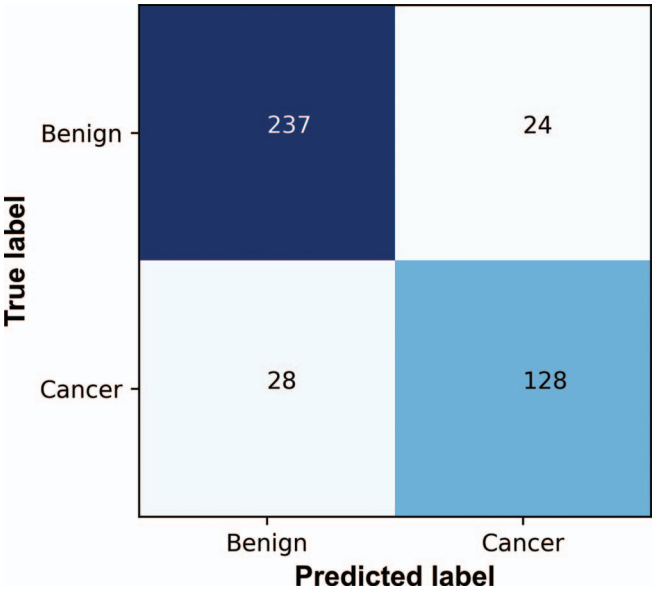

Figure 2. *Confusion matrix summarizing classification results on "ground truth data." The numbers of correct and incorrect predictions are summarized with count values for cancer and benign samples.*

We used the trained OncoSight AI classifier to create a heatmap at the full specimen level. This is performed by using a sliding window approach in which we selected a square patch of a specific pixel size. This patch is used as the input for our trained model, and the model calculates the probability of cancer in this patch. The probability score is assigned to the center pixel, the window then slides across all the pixels in the test image to create a probability map. The final probability map is displayed as a heatmap to show cancer probability of 0% to 100% from blue to red.

Figure 3, A, shows a representative heatmap displaying the probability of cancer computed by using the above classifier on a tissue block that did not have any cancer. The corresponding ground truth H&E is shown in Figure 3, B. As evident, the predicted heatmap is in good concordance with the H&E image devoid of identifiable cancer features. The small black points/areas within the cancer probability map represent background or dye correction artifacts.

Figure 4, A, and Figure 5, A, depict the cancer heatmap on histologically confirmed positive IDC blocks along with corresponding H&E images Figure 4, B, and Figure 5, B. The tissue block in Figure 4 was from a 69-year-old woman with grade T2 cancer and known diabetes. The cancer heatmap in Figure 5, A, is generated from another patient's tissue block with no diabetic history and with cancer grade T1. The heatmaps show the presence of cancer on the tissue blocks and spatially correlate well with the corresponding H&E slides.

Figure 6, A, shows cancer heatmap on predominantly ILC block with corresponding H&E image (Figure 6, B). The heatmap indicates the presence of cancer on the tissue block and spatially correlates well with the corresponding H&E slide except for the top right area, which shows false positive. This false positive can be attributed to deformation and distortion of imaged tissue block during FFPE process and microtoming.

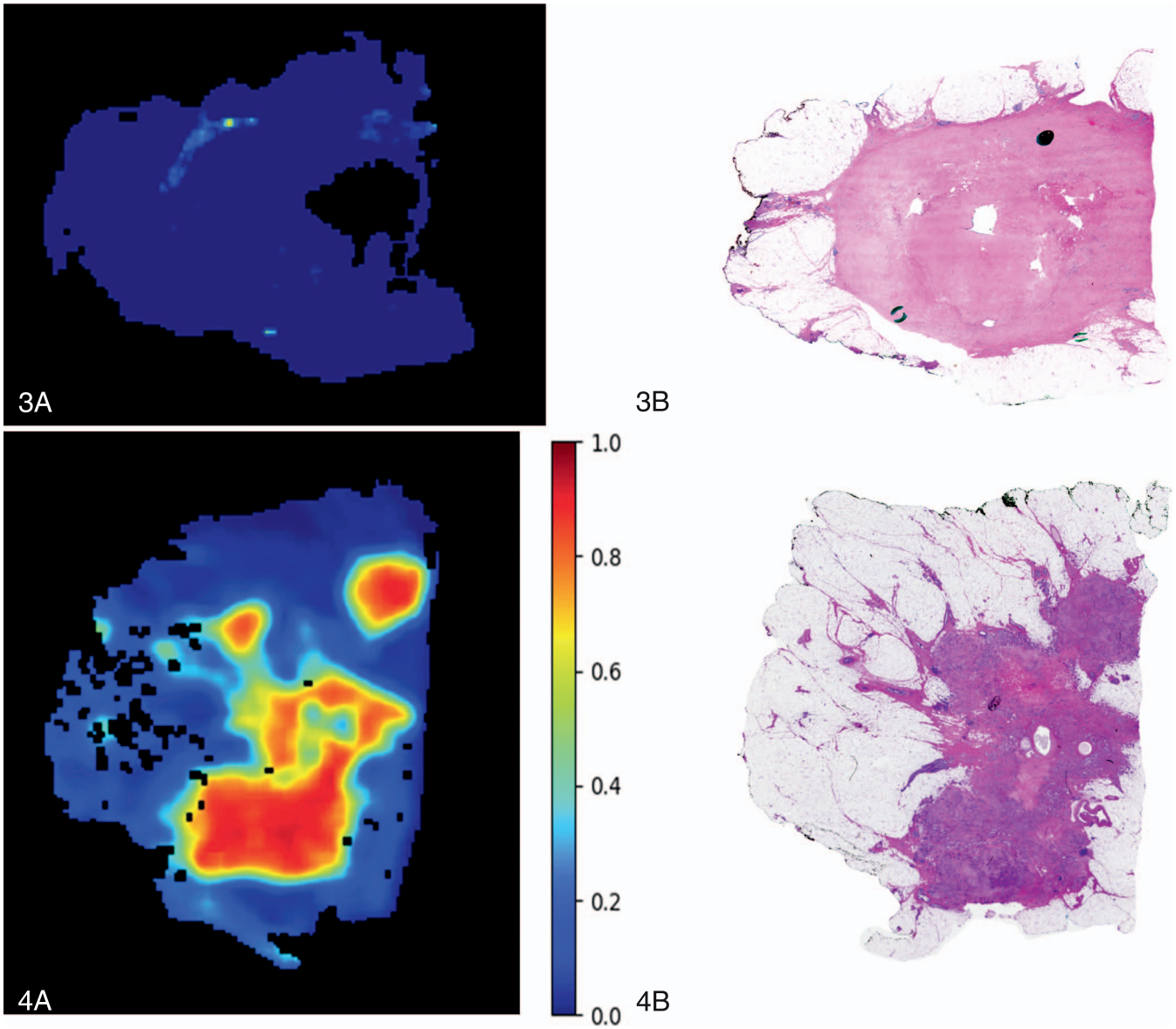

Figure 3. *Probability of cancer generated with OncoSight AI classifier (CytoVeris Inc) trained on panels of multispectral images (A), and hematoxylin-eosin image of histologically confirmed "clear"/negative tissue block (B).*

Figure 4. *Probability of cancer generated with OncoSight AI (CytoVeris Inc) on a tissue block containing invasive ductal carcinoma (A), with corresponding hematoxylin-eosin image showing cancer regions (B).*

Figure 7, A, shows cancer heatmap on a tissue block containing DCIS and compared with the corresponding H&E image from the same block in Figure 7, B. The heatmap shows the presence of cancer on the tissue block and spatially correlates with the corresponding H&E slide.

Figure 8 presents the receiver operating characteristic (ROC) curve for the ensemble classifier for neoplasm detection. The ROC curve plots sensitivity (true positive rate) versus false-positive rate (1 − specificity) for the decision algorithm as the discrimination threshold is varied. The area under the curve is computed to be 0.92.

DISCUSSION

We have developed a label-free optical imaging platform that exploits the endogenous multispectral AF contrast of tissue to discern neoplasms. The AF images reveal a different biomolecular composition at each location in the images and quantitative analysis of this spatial-spectral content of tissue provides richer information than the fluorescence spectrum. The advent and availability of UVC LEDs, advancements in UV filter technology, and the emergence of AI have recently enabled full exploitation of the rich optical contrast of biomolecular fluorophores embedded in tissues. The underlying rationale for AF imaging-based tissue analysis is that multispectral AF images would provide a snapshot of the integral information of tissue fluorophores and, when combined with advanced ML, would capture latent biomolecular and morphologic differences that are encoded in the multispectral images.

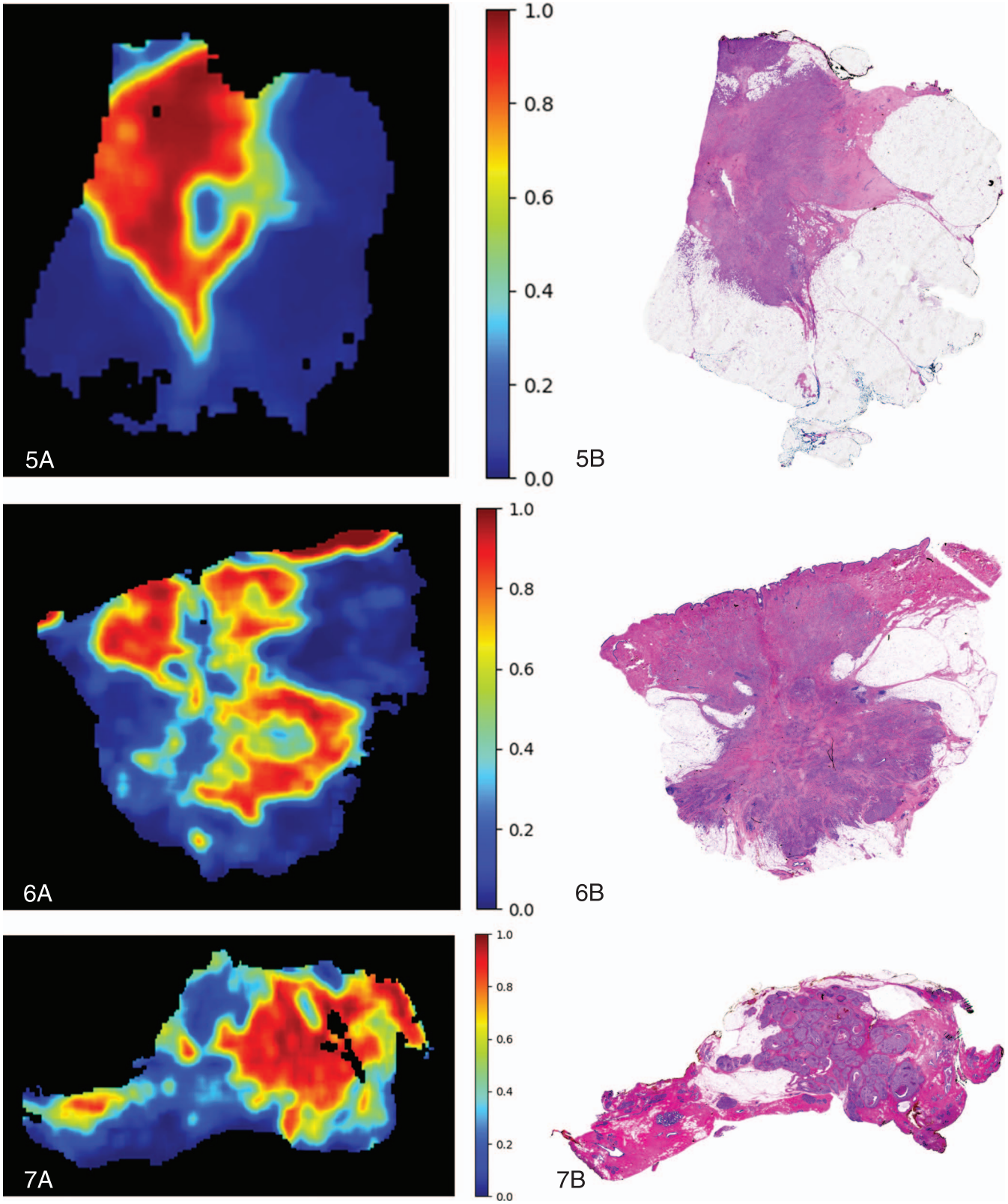

Figure 5. *Probability of cancer generated with OncoSight AI (CytoVeris Inc) on a tissue block containing invasive ductal carcinoma (A), with corresponding hematoxylin-eosin image (B).*

Figure 6. *Probability of cancer generated with OncoSight AI (CytoVeris Inc) on a tissue block with invasive lobular carcinoma (A), with corresponding hematoxylin-eosin image (B).*

Figure 7. *Probability of cancer generated with OncoSight AI (CytoVeris Inc) on a tissue block containing ductal carcinoma in situ (A), with corresponding hematoxylin-eosin image (B).*

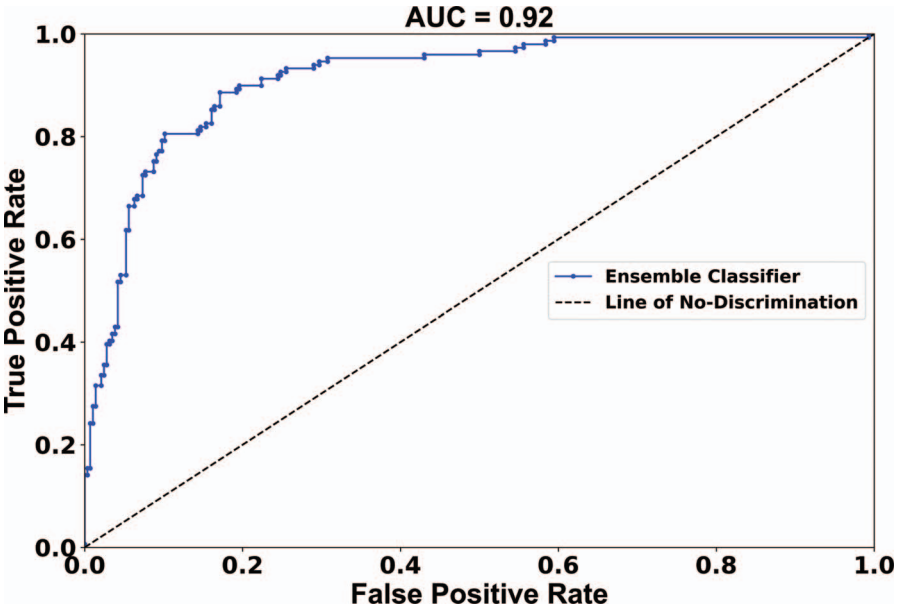

Figure 8. *Receiver operating characteristic curve for the classifier, using OncoSight AI (CytoVeris Inc). Abbreviation: AUC, area under the curve.*

In terms of clinical applications, fundus AF imaging is a routinely used diagnostic tool in ophthalmology.[39] Another AF-based device, the PTeye[40] system, has been cleared by the FDA to aid surgeons in the identification of parathyroid tissue during thyroid and parathyroid surgery. Further, the feasibility of tissue AF imaging has been established in clinical studies for real-time sampling and treatment guidance of bioburden in chronic wounds.[41] Apart from the surgical space, AF microscopy has been used in the last few years in conjunction with a deep learning framework to create virtual histologic images.[42,43] However, prior work using AF to discriminate BCS has been limited, relying on fiber probes and using simpler data analysis tools. Our imaging platform effectively and optimally uses the comprehensive and rich biomolecular information embedded in the tissue matrix both from cells and the extracellular matrix and offers a potentially transformative assessment tool by using the prior rigor of research in AF of tissue and exploiting the very recent advancement in UV LEDs and AI/ML framework.

Other device-based intraoperative methods used in BCS include specimen imaging by radiography and by intraoperative ultrasonography. These devices provide some information about the tissue microstructure. Presently, the interpretation of these outputs requires trained personnel (a radiologist). A hand-held device called MarginProbe (Dilon Technologies, Inc.) that uses dielectric spectroscopy to characterize tissue has been marketed for BCS margin detection. In its pivotal clinical study, MarginProbe demonstrated margin level device sensitivity of 75% and margin level specificity of 46% with a positive predictive value of 22% and a negative predictive value of 90%. The standard-of-care arm (ie, not aided by the device) recorded a sensitivity of 34%, a specificity of 83%, a positive predictive value of 30%, and a negative predictive value of 86%.[44] As reported by LeeVan et al,[45] the MarginProbe, when used as an adjunct to the standard operating procedure, does not significantly reduce re-excision rates in the BCS.

There are 4 principal advantages of the TumorMAP system: First, it is widefield imaging and therefore allows near real-time detection. Second, it provides comprehensive multispectral information that is interpretable and attributable to the known biology and biochemical factors associated with normal and malignant tissue. Third, a successful demonstration of this approach will pave the way for the realization of an accurate and label-free device for neoplasm detection in the OR and in pathology. Fourth, its cost-effectiveness and ease of use have the potential to make effective BCS surgery more accessible to people not served by major cancer centers.

The classification results shown in Figure 2 are very encouraging. These models are trained and tested on highly homogeneous data, and we achieved a classification accuracy of 88%. As illustrated in the confusion matrix, TumorMAP missed 28 tiles from 21 patients and 1 patient was without a grade being DCIS. Of 20 patients with histologic grades, 5 patients had grade I (Nottingham score 3–5) cancer, 11 patients had grade II cancer, and 4 patients had grade III. We do not observe any marked association of false-negative rate with cancer grade in view of a total number of patients with various Nottingham scores as mentioned in the Table—grade I: 11, grade II: 29, grade III: 10 patients.

Several inherent and known errors are attributable to diminished classification performance. Error in the spatial registration of the AF image with the H&E image presents a significant challenge owing to distortion and deformation of tissue during the FFPE process and is a major source of error. Further, registration errors in the Z-axis due to microtoming is inevitable given ~100-mm penetration depth of UV light and the routine trimming of paraffin-embedded tissue blocks for obtaining a flat tissue surface. Furthermore, while we had applied dye masks and corrected for the dye signals, either the residual uncorrected dye signal or artifacts due to correction could have introduced a confounding emission signal into the tissue AF data.

The cancer heatmaps shown in Figures 4 through 7 underscore that our TumorMAP system successfully detects different kinds of cancer. We have trained and tested 156 cancer tiles from 55 patients and the classification accuracies for IDC, ILC, and DCIS were 84% [101 of 120 tiles], 72% [18 of 25], and 82% [9 of 11], respectively. The low classification

performance for ILC can be attributed to its unique morphologic characteristics and growth pattern with dyscohesive cells dispersed diffusely in the fibroconnective stroma without eliciting a desmoplastic host stromal response unlike IDC.

While these results showcase the capability of the TumorMAP system and show encouraging indications for its clinical utility in the pathology laboratory for triaging the sample, it is worth noting the limitations of the present proof-of-principle study for application in surgery. First, the data sets used for training and testing in this study were of a high homogeneity threshold and it is yet to be seen how the OncoSight AI classier performs on a mixed tissue sample. Second, we have measured only 2D tissue blocks in the grossing laboratory and the system and algorithm results must be evaluated on freshly excised 3D tissue. Third, our malignant class did not include rare cancer types, such as mucinous carcinoma and sarcoma, owing to the prevalence and high cancer homogeneity threshold used in this study. We plan to address all the above issues in our planned intraoperative feasibility study.

Taken together, we have demonstrated that the TumorMAP system can accurately discern malignant neoplasm from different types of benign tissues without disruption to the clinical workflow. We are developing and moving to commercialize a cost-effective, intraoperative imaging system for the ex vivo examination of excised specimens. In particular, this label-free approach has unique advantages that allow the assessment of biomolecular and morphologic differences between benign and cancer tissue to assist surgeons in rapidly making intraoperative decisions. Combining the rich biomolecular and morphologic features derived from AF imaging with AI/ML would lead to the next generation of real-time intraoperative assessment, improve efficiencies, and potentially reduce the burden to the patient, surgeon, and pathologist in determining and knowing whether cancer has been left behind.

The authors acknowledge current and former CytoVeris employees for their help in the successful completion of this study. We are thankful to Heather Couture, PhD, for her guidance in classifier development. Finally, we show our appreciation to reviewers for their constructive critique of the manuscript.

References

1. Siegel RL, Miller KD, Fuchs HE, Jemal A. Cancer statistics, 2021. *CA Cancer J Clin*. 2021;71(1):7–33.

2. Fisher B, Anderson S, Bryant J, et al. Twenty-year follow-up of a randomized trial comparing total mastectomy, lumpectomy, and lumpectomy plus irradiation for the treatment of invasive breast cancer. *N Eng J Med*. 2002;347(16):1233–1241.

3. Corradini S, Reitz D, Pazos M, et al. Mastectomy or breast-conserving therapy for early breast cancer in real-life clinical practice: outcome comparison of 7565 cases. *Cancers (Basel)*. 2019;11(2):160.

4. Wilke LG, Czechura T, Wang C, et al. Repeat surgery after breast conservation for the treatment of stage 0 to II breast carcinoma: a report from the National Cancer Data Base, 2004-2010. *JAMA Surg*. 2014;149(12):1296–1305.

5. McCahill LE, Single RM, Bowles EJ Aiello, et al. Variability in reexcision following breast conservation surgery. *JAMA*. 2012;307(5):467–475.

6. Valero MG, Mallory MA, Losk K, et al. Surgeon variability and factors predicting for reoperation following breast-conserving surgery. *Ann Surg Oncol*. 2018;25(9):2573–2578.

7. Mascagni P, Longo F, Barberio M, et al. New intraoperative imaging technologies: innovating the surgeon's eye toward surgical precision. *J Surg Oncol*. 2018;118(2):265–282.

8. Maloney BW, McClatchy DM, Pogue BW, Paulsen KD, Wells WA, Barth RJ. Review of methods for intraoperative margin detection for breast conserving surgery. *J Biomed Opt*. 2018;23(10):100901.

9. Brown JQ, Bydlon TM, Richards LM, et al. Optical assessment of tumor resection margins in the breast. *IEEE J Sel Top Quantum Electron*. 2010;16(3):530–544.

10. Nguyen QT, Tsien RY. Fluorescence-guided surgery with live molecular navigation—a new cutting edge. *Nat Rev Cancer*. 2013;13(9):653–662.

11. Tummers QR, Verbeek FP, Schaafsma BE, et al. Real-time intraoperative detection of breast cancer using near-infrared fluorescence imaging and Methylene Blue. *Eur J Surg Oncol*. 2014;40(7):850–858.

12. Unger J, Hebisch C, Phipps JE, et al. Real-time diagnosis and visualization of tumor margins in excised breast specimens using fluorescence lifetime imaging and machine learning. *Biomed Opt Express*. 2020;11(3):1216–1230.

13. Smith BL, Gadd MA, Lanahan CR, et al. Real-time, intraoperative detection of residual breast cancer in lumpectomy cavity walls using a novel cathepsin-activated fluorescent imaging system. *Breast Cancer Res Treat*. 2018;171(2):413–420.

14. Tao YK, Shen D, Sheikine Y, et al. Assessment of breast pathologies using nonlinear microscopy. *Proc Natl Acad Sci U S A*. 2014;111(43):15304–15309.

15. de Boer LL, Bydlon TM, van Duijnhoven F, et al. Towards the use of diffuse reflectance spectroscopy for real-time in vivo detection of breast cancer during surgery. *J Transl Med*. 2018;16(1):367.

16. Haka AS, Volynskaya Z, Gardecki JA, et al. Margin assessment during partial mastectomy breast surgery using raman spectroscopy. *Cancer Res*. 2006;66(6):3317.

17. Zúñiga WC, Jones V, Anderson SM, et al. Raman spectroscopy for rapid evaluation of surgical margins during breast cancer lumpectomy. *Sci Rep*. 2019;9(1):14639.

18. Kho E, de Boer LL, Van de Vijver KK, et al. Hyperspectral imaging for resection margin assessment during cancer surgery. *Clin Cancer Res*. 2019;25(12):3572–3580.

19. Schmidt H, Connolly C, Jaffer S, et al. Evaluation of surgically excised breast tissue microstructure using wide-field optical coherence tomography. *Breast J*. 2020;26(5):917–923.

20. Kennedy KM, Zilkens R, Allen WM, et al. Diagnostic accuracy of quantitative micro-elastography for margin assessment in breast-conserving surgery. *Cancer Res*. 2020;80(8):1773.

21. Zhang RR, Schroeder AB, Grudzinski JJ, et al. Beyond the margins: real-time detection of cancer using targeted fluorophores. *Nat Rev Clin Oncol*. 2017;14(6):347–364.

22. Pogue BW, Rosenthal EL, Achilefu S, van Dam GM. Perspective review of what is needed for molecular-specific fluorescence-guided surgery. *J Biomed Opt*. 2018;23(10):1–9.

23. Ostrander JH, McMahon CM, Lem S, et al. Optical redox ratio differentiates breast cancer cell lines based on estrogen receptor status. *Cancer Res*. 2010;70(11):4759.

24. Croce AC, Bottiroli G. Autofluorescence spectroscopy and imaging: a tool for biomedical research and diagnosis. *Eur J Histochem*. 2014;58(4):2461.

25. Palmer GM, Changfang Z, Breslin TM, Fushen X, Gilchrist KW, Ramanujam N. Comparison of multiexcitation fluorescence and diffuse reflectance spectroscopy for the diagnosis of breast cancer (March 2003). *IEEE Trans Biomed Eng*. 2003;50(11):1233–1242.

26. Saraswathy A, Jayasree RS, Baiju KV, Gupta AK, Pillai VPM. Optimum wavelength for the differentiation of brain tumor tissue using autofluorescence spectroscopy. *Photomed Laser Surg*. 2008;27(3):425–433.

27. Zheng W, Lau W, Cheng C, Soo KC, Olivo M. Optimal excitation-emission wavelengths for autofluorescence diagnosis of bladder tumors. *Int J Cancer*. 2003;104(4):477–481.

28. Marsden M, Weyers BW, Bec J, et al. Intraoperative margin assessment in oral and oropharyngeal cancer using label-free fluorescence lifetime imaging and machine learning. *IEEE Trans Biomed Eng*. 2021;68(3):857–868.

29. Wang M, Long F, Tang F, et al. Autofluorescence imaging and spectroscopy of human lung cancer. *Appl Sci*. 2017;7(1):32.

30. Gorpas D, Phipps J, Bec J, et al. Autofluorescence lifetime augmented reality as a means for real-time robotic surgery guidance in human patients. *Sci Rep*. 2019;9(1):1187.

31. Dance A. AI spots cell structures that humans can't. *Nature*. 2021;592(7852):154–155.

32. Christiansen EM, Yang SJ, Ando DM, et al. In silico labeling: predicting fluorescent labels in unlabeled images. *Cell*. 2018;173(3):792–803.e19.

33. Savage N. How AI is improving cancer diagnostics. *Nature*. 2020;579(7800):S14–S16.

34. Kim HE, Kim HH, Han BK, et al. Changes in cancer detection and false-positive recall in mammography using artificial intelligence: a retrospective, multireader study. *Lancet Digit Health*. 2020;2(3):e138–e148.

35. Chang HY, Jung CK, Woo JI, et al. Artificial intelligence in pathology. *J Pathol Transl Med*. 2019;53(1):1–12.

36. Yala A, Lehman C, Schuster T, Portnoi T, Barzilay R. A deep learning mammography-based model for improved breast cancer risk prediction. *Radiology*. 2019;292(1):60–66.

37. Harrison JH, Gilbertson JR, Hanna MG, et al. Introduction to artificial intelligence and machine learning for pathology. *Arch Pathol Lab Med*. 2021;145(10):1228–1254.

38. Chicco D, Tötsch N, Jurman G. The Matthews correlation coefficient (MCC) is more reliable than balanced accuracy, bookmaker informedness, and markedness in two-class confusion matrix evaluation. *BioData Min*. 2021;14(1):13.

39. Sepah YJ, Akhtar A, Sadiq MA, et al. Fundus autofluorescence imaging: fundamentals and clinical relevance. *Saudi J Ophthalmol*. 2014;28(2):111–116.

40. Thomas G, McWade MA, Nguyen JQ, et al. Innovative surgical guidance for label-free real-time parathyroid identification. *Surgery*. 2019;165(1):114–123.
41. DaCosta RS, Kulbatski I, Lindvere-Teene L, et al. Point-of-care autofluorescence imaging for real-time sampling and treatment guidance of bioburden in chronic wounds: first-in-human results. *PLoS One*. 2015;10(3):e0116623.
42. Rivenson Y, Wang H, Wei Z, et al. Virtual histological staining of unlabelled tissue-autofluorescence images via deep learning. *Nat Biomed Eng*. 2019;3(6):466–477.
43. Rivenson Y, de Haan K, Wallace WD, Ozcan A. Emerging advances to transform histopathology using virtual staining. *BME Frontiers*. 2020;2020:9647163.
44. *FDA Summary of Safety and Effectiveness Data, MarginProbe System, PMA P110014*. Silver Spring, MD: FDA; 2012.
45. LeeVan E, Ho BT, Seto S, Shen J. Use of MarginProbe as an adjunct to standard operating procedure does not significantly reduce re-excision rates in breast conserving surgery. *Breast Cancer ResTreat*. 2020;183(1):145–151.